RSC Advances

PAPER

View Article Online
View Journal | View Issue

Cite this: *RSC Adv.*, 2019, **9**, 25471

The excellent TE performance of photoelectric material CdSe along with a study of Zn(Cd)Se and Zn(Cd)Te based on first-principles†‡

Qi Zhong,[a] Zhenhong Dai, *[a] Jianye Liu,[a] Yinchang Zhao [a] and Sheng Meng [b]

Zn(Cd)Se and Zn(Cd)Te are well known for their excellent photoelectric performance, however, their thermoelectric (TE) properties are usually ignored. By taking advantage of first-principles calculations, the Boltzmann transport equation and semiclassical analysis, we executed a series of thermal and electronic transport investigations on these materials. Our results show that CdSe has the lowest anisotropic thermal conductivity, κ_L, of the four materials, at 4.70 W m^{-1} K^{-1} (*c* axis) and 3.85 W m^{-1} K^{-1} (*a* axis) at a temperature of 300 K. Inspired by the very low lattice conductivity, other thermoelectric parameters were calculated in the following research. At a temperature of 1200 K we obtained a pretty large power factor, $S^2\sigma$, of 4.39 × 10^{-3} W m^{-1} K^{-2}, and based it on the fact that the corresponding figure of merit *ZT* can reach 1.8 and 1.6 along the *a* axis and *c* axis, respectively. We revealed the neglected thermoelectric potential of CdSe by means of systematic studies and demonstrated that it is a promising material with both excellent photoelectric performance and thermoelectric performance.

Received 24th June 2019
Accepted 26th July 2019

DOI: 10.1039/c9ra04748d

rsc.li/rsc-advances

1. Introduction

With increasing environmental pollution, searching for alternative energy and recovering waste heat more effectively have become urgent problems to be solved. Thermoelectric (TE) materials make it possible to convert heat energy into electric energy with no pollution in this process.[1–4] What is used to evaluate thermoelectric materials is the dimensionless figure of merit $ZT = S^2\sigma T/(\kappa_e + \kappa_L)$,[5] where S, σ, T, κ_e and κ_L are the thermopower (Seebeck coefficient), electrical conductivity, absolute temperature, electrical thermal conductivity and lattice thermal conductivity, respectively. In terms of the formula above, increasing the power factor $S^2\sigma$ and decreasing the lattice thermal conductivity are two measures usually used to improve *ZT*.[1,6–12] Making use of the carrier scattering mechanism,[13,14] modulation doping[15] and band engineering,[11,16,17] the power factor $S^2\sigma$ can be improved effectively. The lattice thermal conductivity κ_L can be shown as $\kappa_L = C_V\nu_{ph}l/3$, where C_V, l and ν_{ph} are the heat capacity, phonon mean free path and phonon group velocity, respectively. By utilizing microstructure defects and nanostructures[18–21] the κ_L can be significantly reduced, for example CaF_2, SrF_2 and BaF_2 crystals, with a fluorite structure (space group $Fm\bar{3}m$), acquired a substantially decreased thermal conductivity by doping with rare-earth elements,[22–24] and the p-type nanocrystalline bismuth antimony telluride (BiSbTe) bulk material showed a peak *ZT* of 1.2 at room temperature by the increased phonon scattering by defects and grain boundaries.[20] In view of the above, similar methods can be applied to selenide and telluride.

Organic materials, especially polymer materials, have been found to be one of the best potential thermoelectric materials on account of their excellent flexibility, easy production, as well as high power factor,[25] but the poor thermal stability and high contact resistance restrict their application in the commercial field.[26] Based on the above, the thermoelectric materials applied in practice are mainly inorganic compounds, such as Na-doped PbTe (*ZT* ∼ 2.0 at 773 K), for which the κ_L was reduced by adjusting the nanostructure,[7] heavily doped PbSe[27] (*ZT* ∼ 2.0 at 1000 K), p-type GBT compounds $[GeTe]_m[Bi_2Te_3]_n$[28] (*ZT* ∼ 1.4 at 300 K), n-type doped SnSe[29] (*ZT* ∼ 2.7 along the *a* axis) and Cu_2Se, for which the *ZT* values were enhanced by doping with 1 mol% indium and a peak value of 2.6 at 850 K was achieved.[30] Additionally, studies by the Ren group and Tritt group[20,31] have recently acquired *ZT* values of 1.5 in nanostructured Bi_2Te_3 accompanied with a reduced lattice thermal conductivity, enhanced Seebeck coefficient S and enhanced mobility μ.

From the above materials we can see that they all contain Se or Te in the compounds and so in this paper we investigated ZnSe, ZnTe, CdSe and CdTe which have been usually researched for their excellent optical properties,[32,33] but their thermoelectric properties were easily neglected. Generally speaking, direct

[a]*Department of Physics, Yantai University, Yantai 264005, People's Republic of China. E-mail: zhdai@ytu.edu.cn; y.zhao@ytu.edu.cn*

[b]*Beijing National Laboratory for Condensed Matter Physics and Institute of Physics, Chinese Academy of Sciences, Beijing, 100190, People's Republic of China. E-mail: smeng@iphy.ac.cn*

† PACS numbers: 65.40.-b, 66.70.-f, 63.20.-e, 72.20.-i.

‡ Electronic supplementary information (ESI) available. See DOI: 10.1039/c9ra04748d

band gap semiconductors are more suitable for photoelectric materials, while indirect band gap semiconductors with a moderate band gap are more likely to be chosen for thermoelectric materials. This is because for indirect band gap semiconductors the conduction band minimum and valence band maximum are located in different positions in κ space, thus they not only require energy absorption but also a change in momentum to complete the transition of electrons. However, the band gap is not the only factor that determines the properties of thermoelectric materials: the electronic band structures, electronic effective mass, Debye temperature Θ_D, phonon group velocities and scattering rate also play a role. In this paper, we carried out first-principles calculations and systematically studied the electronic and thermal transport properties of those materials and surprisingly found that all of them have relatively low lattice thermal conductivity, especially CdSe. In view of this, we calculated the power factor, electronic thermal conductivity and figure of merit *ZT* of CdSe and obtained a glorious result, which confirms that CdSe not only performs well in the field of photoelectricity, but also shows superior performance in thermoelectric devices. In Sec. 2, we introduce the calculation methods and some details. In Sec. 3, the calculated data and some figures are shown. Sec. 4 is the summery of our work.

2. Methodology

The lattice thermal conductivity κ_L is an important parameter in the process of investigating thermal transport properties, which can be obtained from the phonon Boltzmann transport equation (BTE) and the interatomic force constant (IFC), and along the α axis κ_L is defined as:

$$\kappa_L{}^{\alpha\alpha} = \frac{1}{k_B T^2 \Omega N_q} \sum_{q\nu} n_{q\nu}(n_{q\nu}+1)(\hbar\omega_{q\nu})^2 \nu_{q\nu}{}^{\alpha} F_{q\nu}{}^{\alpha}, \quad (1)$$

where κ_B, Ω, N_q, $n_{q\nu}$ and $\nu^{\alpha}_{q\nu}$ are the Boltzmann constant, unit cell volume, quantity of q points in the Brillouin zone (BZ), equilibrium Bose–Einstein distribution function and phonon group velocities along the direction of the α axis, respectively. In the above equation,

$$F_{q\nu}{}^{\alpha} = \tau^{ph}_{q\nu}(\upsilon_{q\nu}{}^{\alpha} + \Delta_{q\nu}) \quad (2)$$

where $\tau^{ph}_{q\nu}$ and $\Delta_{q\nu}$ are the phonon relaxation time of mode qν with the relaxation time approximation (RTA) and the correction term of RTA, respectively. In order to acquire the *ZT* values we used the electron Boltzmann theory,[34] and at the same time, the thermopower *S*, electronic thermal conductivity κ_e and electrical conductivity σ can be obtained in the process of investigating the electronic transport properties as follows:[35]

$$S_{\alpha\alpha} = -\frac{1}{eT} \frac{\sum_{nk}(\varepsilon_{nk}-\varepsilon_F)(\upsilon_{nk}{}^{\alpha})^2 \tau^{el}_{nk} \frac{\partial f_{nk}}{\partial \varepsilon_{nk}}}{\sum_{nk}(\upsilon_{nk}{}^{\alpha})^2 \tau^{el}_{nk} \frac{\partial f_{nk}}{\partial \varepsilon_{nk}}} \quad (3)$$

$$\sigma_{\alpha\alpha} = -\frac{e^2}{N_k \Omega} \sum_{nk} (\upsilon_{nk}{}^{\alpha})^2 \tau^{el}_{nk} \frac{\partial f_{nk}}{\partial \varepsilon_{nk}} \quad (4)$$

$$\kappa_e{}^{\alpha\alpha} = -\frac{1}{N_k \Omega T} \sum_{nk} (\varepsilon_{nk}-\varepsilon_F)^2 (\upsilon_{nk}{}^{\alpha})^2 \tau^{el}_{nk} \frac{\partial f_{nk}}{\partial \varepsilon_{nk}} - T S_{\alpha\alpha}{}^2 \sigma_{\alpha\alpha} \quad (5)$$

where ε_F, N_k, ε_{nk}, f_{nk}, υ^{α}_{nk} and τ^{el}_{nk} are the Fermi energy, amount of k points in the BZ, energy eigenvalue of state nk, Fermi–Dirac distribution function, electron group velocities along the direction of the α axis and electron lifetime, respectively.

In the course of calculating the *ZT* values, lattice thermal transport and electronic transport are two parts that we should focus on. For the lattice thermal transport study, κ_L was calculated by the SHENGBTE code[36] with a 15 × 15 × 15 *q*-mesh taken from the BZ. Using a 3 × 3 × 3 supercell, the IFC2 and IFC3 are computed with a combination of the VASP package,[37,38] PHONOPY program[39] and THIRDORDER.PY script.[36] For optimizing the initial cell, take 9 × 9 × 9 *Γ*-centered Monkhorst–Pack *k*-mesh from the BZ and the ion (electronic) convergence criterion is 10^{-6} eV (10^{-8} eV), the interactions between ion cores and valence electrons are modeled by the projector augmented wave potentials (PAW)[40] and a plane wave basis set with a cutoff energy of 500 eV is used. The generalized gradient approximation (GGA) of Perdew–Burke–Ernzerhof (PBE) was applied in the exchange-correlation functional.[41] In terms of electronic transport, using the semiclassical Boltzmann theory, rigid-band method and constant scattering time approximation, κ_e, σ and *S* can be obtained using the BOLTZTRAP code.[42] Additionally, for the purpose of acquiring Kohn–Sham eigenvalues derivatives, a 55 × 55 × 55 *k*-mesh of BZ is used in the process of optimizing the electronic structure. In the process of DFT calculations, the lattice constant *a* (*c*) is for the ground-state systems, which eliminated the effect of thermal expansion (TE) caused by the lattice vibrations (effect of crystal volume change on phonon frequency), however, the TE effect in heavy materials is fairly weak[43] and the materials we study all have large atomic masses similarly to the thermoelectric studies of HgS,[35] SnGe,[44] $CoSb_3$ and $IrSb_3$,[45] all of which neglected the TE effect. Additionally, ZnSe, CdSe, ZnTe and CdTe are not layered materials in view of their crystal structures (shown in Fig. 1) so we don't use the vdW corrections.

3. Results and discussion

Fig. 1 and Table 1 show the crystal and electronic band structures and calculated parameters of ZnSe, CdSe, ZnTe and CdTe, respectively. Fig. 1(a) and (b) are the crystal structures of these materials, and Zn(Cd)Se and Zn(Cd)Te belong to the hexagonal and cubic crystal systems with an anisotropic and isotropic lattice structure, respectively, which influences the electronic structure and transport properties. The primitive cell of ZnSe (CdSe) is composed of two Zn (Cd) atoms and two Se atoms, and in the case of the ZnTe (CdTe) primitive cell, it is constituted by four Zn (Cd) atoms and four Te atoms. The space group and computed equilibrium lattice constant and band gap are consistent with previous work[46–51] and are shown in Table 1. We also calculated the electronic band structures using the GW

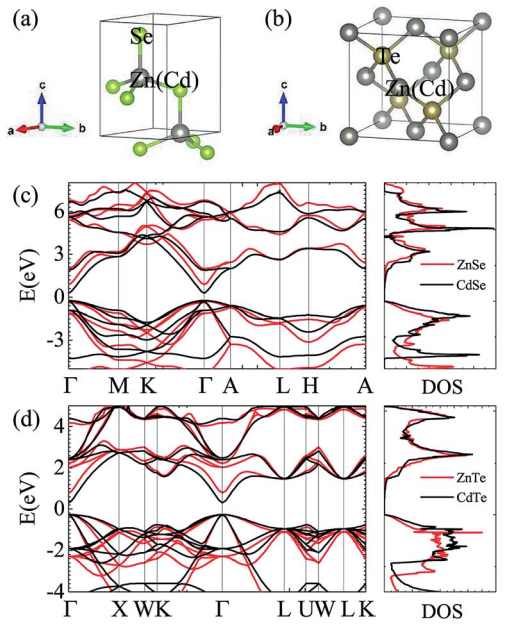

Fig. 1 Crystal structures of ZnSe and CdSe (a) and ZnTe and CdTe (b). Electronic band structures and total electron density of states (DOS) along different high-symmetry paths within the first Brillouin zone of ZnSe and CdSe (c) and ZnTe and CdTe (d).

Table 1 Space group and calculated equilibrium Lattice constant(s) and band gap for ZnSe, CdSe, ZnTe and CdTe

Material	Space group	a (Å)	c (Å)	E_g (eV)
ZnSe	$P6_3mc$[186]	4.051	6.656	1.18
CdSe	$P6_3mc$[186]	4.392	7.167	0.53
ZnTe	$F\bar{4}3m$[216]	6.185	—	1.06
CdTe	$F\bar{4}3m$[216]	6.625	—	0.57

approximation, which is consistent with previous research:[52] the scissors shift of $E_{GW} - E_{DFT}$ has no effect on the thermal transport properties of these materials. From Fig. 1(c) and (d), we can see that all of the four materials are direct band gap semiconductors, with the band gap of ZnSe (ZnTe) generally larger than that of CdSe (CdTe). The local band effective mass m_b^* is closely related to the band shape, which is defined as:

$$m_b^* = \hbar^2 \left(\frac{\partial^2 E(\kappa)}{\partial \kappa^2} \right)^{-1} \quad (6)$$

where $\hbar$, $E(\kappa)$ and κ are the reduced Planck constant, energy dispersion function and wave vector, respectively. Often, a large Seebeck coefficient is derived from a flat band shape (signifies a large effective mass) and a favorable dispersion at the bottom of the conduction band, as shown in Fig. 1(c) and (d), and these four materials all meet the requirements. In addition, the electronic band structure shows a conical band energy dispersion (Dirac states) due to the strong spin orbit coupling offered by Se/Te, however, they are only commonplace Dirac states as band-inversion will not occur after the calculation of SOC. According to this study of spin–orbit coupling in tellurides[53] charge carrier accumulation occurs near the conduction band minima, which promotes its thermoelectric efficiency.

For the sake of performing a comprehensive research on the phonon transport properties, the phonon dispersion and phonon density of states (PDOS) are demonstrated in Fig. 2. There are four and eight atoms in the primitive cell of Zn(Cd)Se and Zn(Cd)Te, respectively, so 12 or 24 phonon branches exist in the corresponding picture. Classically, low-frequency phonon modes are primarily derived from the larger atomic mass which is opposite to the situation of high-frequency branches, however, the cases of ZnSe (a) and CdTe (d) are contrary to this rule: the vibrations of heavier atoms (Se or Te) offered the high-frequency phonon modes, and the low-frequency branches are afforded by the lighter atoms (Zn or Cd). We can see that in (b) and (c) the optical modes are split into two parts, which causes a vacancy around the frequency of 4 THz. This phenomenon can also be reflected in the PDOS with the corresponding value equalling zero for CdSe (ZnTe) and the optical modes with frequencies above and below 4 THz have six and three (fifteen and six) branches, respectively. The Debye temperature Θ_D is a significant parameter in terms of thermal transport – at a given temperature a lower Θ_D may cause enhanced phonon scattering so that the lattice conductivity is reduced,[54–56] and this is defined as:

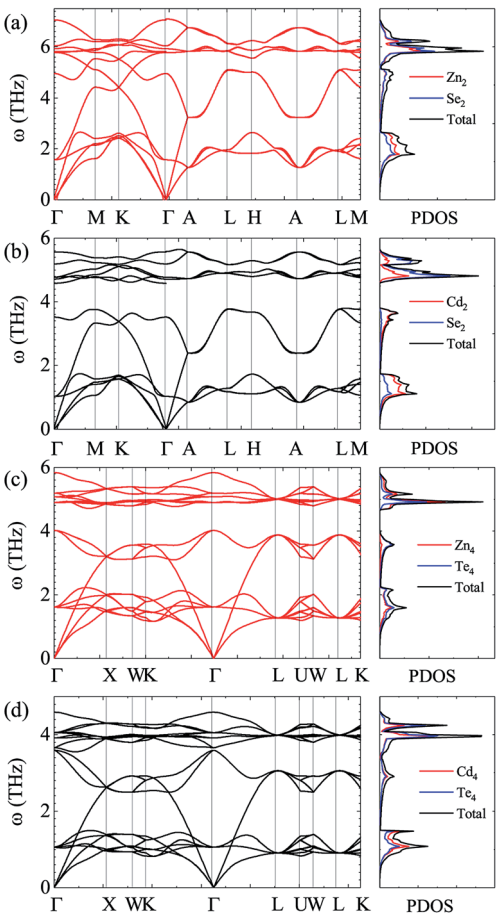

Fig. 2 Calculated phonon dispersion and partial phonon density of states (PDOS) along various high-symmetry paths in the first Brillouin zone of ZnSe (a), CdSe (b), ZnTe (c) and CdTe (d).

$$\Theta_D = \frac{h\nu_m}{\kappa_B} \quad (7)$$

where ν_m, h, κ_B are the highest frequency of atom elastic vibration, Planck constant, and Boltzmann constant, respectively. By calculation, the Debye temperatures Θ_D of ZnSe, CdSe, ZnTe and CdTe are 244 K, 180 K, 186 K and 146 K, respectively. All of them are under room temperature and much lower than 500 K for monolayer MoS_2 and blue phosphorene,[57] and 2300 K for graphene.[58] Compared with ZnSe and ZnTe, CdSe and CdTe have relatively lower Debye temperatures, which means that they may have lower lattice thermal conductivity. In order to verify this conjecture, we carry out the following studies.

Fig. 3 shows the calculated lattice thermal conductivity κ_L and the normalized κ_L *vs.* the phonon maximum mean-free path (MFP) at different temperatures for ZnSe, CdSe, ZnTe and CdTe. Because ZnSe and CdSe are anisotropic, Fig. 3(a) and (c) reveal the data along the *a* axis and *c* axis. Comparing (a) with (b), we find that CdSe and CdTe have lower lattice conductivities, consistent with the above guess. To cite an instance, at the temperature of 300 K, the κ_L values of ZnSe *a* axis (*c* axis), CdSe *a* axis (*c* axis), ZnTe and CdTe are 12.92 W m^{-1} K^{-1} (14.99 W m^{-1} K^{-1}), 3.85 W m^{-1} K^{-1} (4.70 W m^{-1} K^{-1}), 15.86 W m^{-1} K^{-1} and 6.14 W m^{-1} K^{-1}, respectively. All of them are much smaller than the κ_L of graphene (64.80 W m^{-1} K^{-1})[59] and silicene (27.7 W m^{-1} K^{-1}),[60] and some are also lower than $CoSb_3$ (11.5 W m^{-1} K^{-1})[61] and SnSi (10.1 W m^{-1} K^{-1})[44] at the same temperature, especially for CdSe, for which the κ_L along the *a* axis is little smaller than that of SnGe ($\kappa_L \sim 4.7$ W m^{-1} K^{-1} at 300 K, and the *ZT* value reaches 1.64 at 450 K[44]), so it is truly rewarding to further research the thermoelectric properties of it. For the anisotropic material ZnSe (CdSe), the κ_L along the *a* axis is approximately 17.30% ~ 13.20% (19.82% ~ 17.94%) lower than that along *c* axis when the temperature is altered from 100 K to 1000 K, which reflects a moderate anisotropy of the thermal transport properties of ZnSe and CdSe. In Fig. 3(a) and (b), the insets illustrate the relationship between the normalized κ_L and frequency, and it can be summarized that 65% (70%), 95% (94%), 85% and 92% of the κ_L of ZnSe *a* axis (*c* axis), CdSe *a* axis (*c* axis), ZnTe and CdTe, respectively, are provided by the phonon modes with frequencies below 2 THz, where the acoustic modes are located, which means that the acoustic phonons play a dominant role in the process of thermal transport. Fig. 3(c) and (d) reveal the size dependent κ_L – with an increase in temperature the MFP values of all the materials are shortened, which reflects the intensification of phonon activity. At room temperature, when the normalized κ_L reaches 50%, the corresponding phonon MFPs are 72 nm (126 nm), 65 nm (104 nm), 349 nm and 166 nm for ZnSe *a* axis (*c* axis), CdSe *a* axis (*c* axis), ZnTe and CdTe, respectively. Combined with these figures, we can see that CdSe has the shortest MFPs, and in addition, for anisotropic ZnSe and CdSe, compared with the *a* axis the *c* axis has a slightly longer phonon MPF despite the temperature increase. Along with this, the thermal conductivity of chalcogenides can be controlled by the thermally active phonon modes which are affected by defects, as

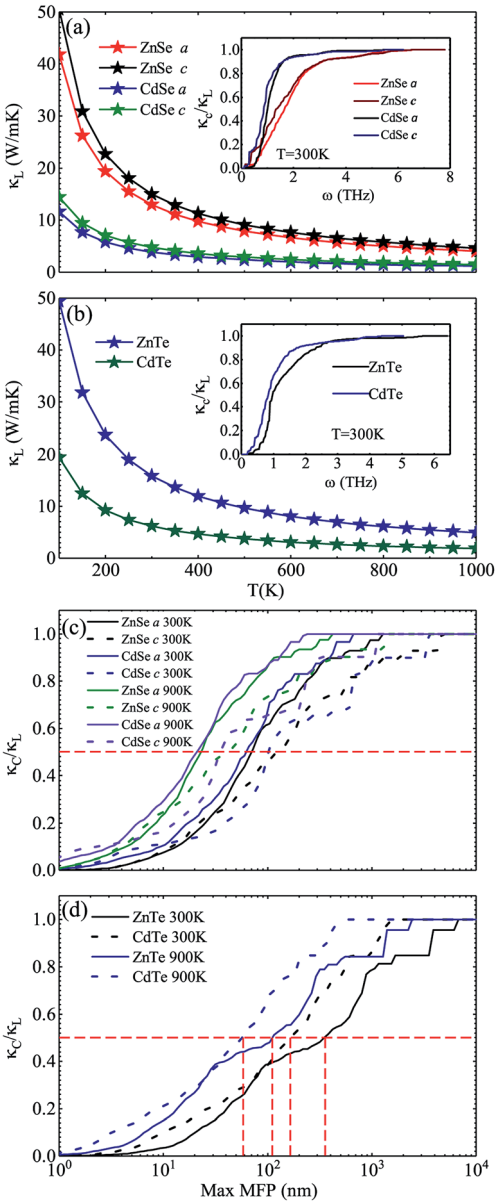

Fig. 3 Calculated Lattice thermal conductivity κ_L of ZnSe and CdSe (a) and ZnTe and CdTe (b), respectively. The insets indicate the normalized κ_L with respect to the frequency, at a temperature of 300 K. In (a), the red pentagram (blue pentagram) and black pentagram (green pentagram) curves represent the κ_L along the *a* axis and *c* axis, respectively. The normalized κ_L *vs.* phonon maximum mean-free path (MFP) at different temperatures for ZnSe and CdSe (c) and ZnTe and CdTe (d). The full line and dotted line represent the results along the *a* axis and *c* axis, respectively.

demonstrated in the instance of Ga doped Cu_2Te, in which within the limits of Ga doping the doping has a great influence on the thermal conductivity: a decreased thermal conductivity κ can be acquired in $Cu_{2-x}Te$ in which intrinsic vacancies were substituted by shallow type dopants of Ga^{3+}. However, if going beyond the doping limits, an increased thermal conductivity can be caused on account of the increased number of thermally active phonon modes in disordered species ($CuGaTe_2$).[62]

To further explore the essence of thermal transport, the phonon group velocities of different phonon modes, and the relevant values along the *a* axis and *c* axis of anisotropic ZnSe and CdSe are shown in Fig. 4. Compared to ZnSe and ZnTe, CdSe and CdTe have the smaller values on the whole, which is consistent with the lower κ_L value of them. In terms of the specific data the largest group velocities of the four materials, all located in the LA modes, are 3.71 Km s^{-1}, 3.14 Km s^{-1}, 4.91 Km s^{-1} and 3.82 Km s^{-1} for ZnTe, CdTe, ZnSe and CdSe, respectively. Considering isotropic ZnTe and CdTe, the group velocities of the acoustic and optical modes show an obvious separation at a frequency around 1 THz, however, a similar phenomenon is not distinct for ZnSe and CdSe, which means that the optical phonons are also involved in the low-frequency thermal transport. The lattice conductivity along the *a* axis is slightly lower than that along the *c* axis for ZnSe and CdSe with regard to Fig. 3, and this point can also be reflected in Fig. 4(e) and (f). Even though the phonon group velocity along the *a* axis is smaller than that along the *c* axis, due to the fact that the differences between them are tiny, the anisotropy of both materials are not obvious.

Judging from the results of the above research, CdSe and CdTe show better thermoelectric properties among the four materials. In order to further reveal the differences between them in thermoelectric performance, the total relaxation time at a temperature of 300 K of acoustic phonons and optical phonons as a function of frequency are shown in Fig. 5(a) and (b), respectively. The acoustic modes of CdTe are mainly concentrated below 1 THz, while CdSe occupies a wider frequency range and has more acoustic modes with relaxation times more than 10 ps, since the acoustic modes account for

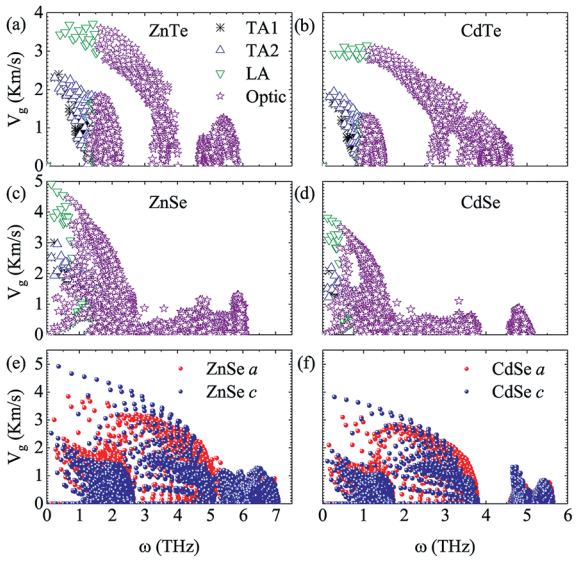

Fig. 4 (a–d) Phonon group velocities as a function of frequency of different phonon modes for ZnSe, CdSe, ZnTe and CdTe. The black, blue, green and purple symbols represent the TA1, TA2, LA and optic modes, respectively. (e and f) are the phonon group velocities with respect to frequency along the *a* axis (red sphere) and *c* axis (blue sphere) of ZnSe and CdSe, respectively.

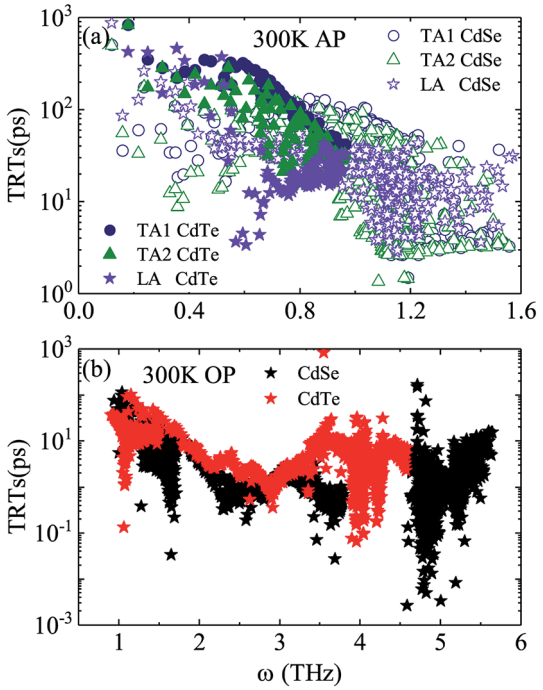

Fig. 5 Total relaxation time as a function of frequency for CdSe and CdTe at a temperature of 300 K. (a) Acoustic phonons (AP) – the solid circle (hollow circle), solid triangle (hollow triangle) and solid pentagram (hollow pentagram) represent the TA1, TA2 and LA modes of CdTe (CdSe), respectively. (b) Optical phonons (OP) – the black and red pentagrams represent the optic modes of CdSe and CdTe, respectively.

only a small fraction of all phonon modes, the conclusions should be drawn from the more convincing Fig. 5(b). The optical modes of CdTe are distributed above those of CdSe over the whole frequency range, which means that the CdTe has a longer relaxation time in the gross and further explains the larger thermal conductivity of it at 300 K. In the following studies, to further explore the physical mechanism involved in thermal transport, the isotopic scattering rates (ISRs), anharmonic three-phonon scattering rates (ASRs), total scattering rates (TSRs) and weighted phase space *W* of acoustic modes and optical modes of CdSe at 300 K are plotted in Fig. 6. The ISRs, ASRs and TSRs are connected by the relaxation time and can be written as:

$$\frac{1}{\tau^{ph}} = \frac{1}{\tau^{anh}} + \frac{1}{\tau^{iso}} \quad (8)$$

where $1/\tau^{ph}$, $1/\tau^{anh}$ and $1/\tau^{iso}$ represent the total scattering rates (TSRs), anharmonic three-phonon scattering rates (ASRs) and isotopic scattering rates (ISRs), respectively. Combining Fig. 6(a–c) with the formula, the verdict can be summarized as the following: the total phonon scattering process is mainly dominated by the anharmonic three-phonon scattering, in the scope of low-frequency, and the scattering rates of optical modes are at least one order of magnitude larger than those of acoustic modes, especially in the process of isotopic scattering, which means that although it is known from Fig. 4 that the optical modes are also related to the low-frequency thermal

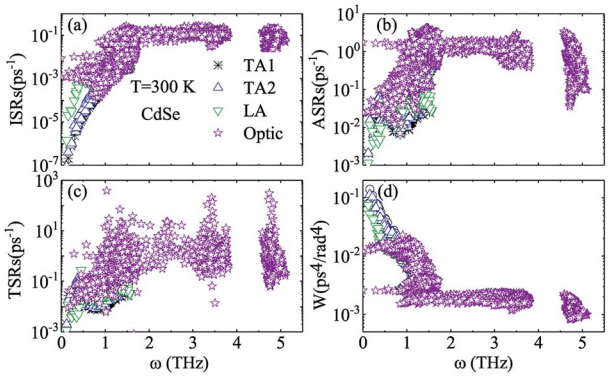

Fig. 6 Isotopic scattering rates (ISRs) (a), anharmonic three-phonon scattering rates (ASRs) (b), total scattering rates (TSRs) (c) and weighted phase space W (d) as a function of frequency at 300 K for CdSe. The black, blue, green and purple symbols represent the TA1, TA2, LA and optic modes of CdSe, respectively.

transport, the lattice thermal conductivity is still mainly contributed to by the acoustic modes. Generally speaking, the anharmonic three-phonon scattering rates (ASRs) stem from the summation of all three-phonon transition probabilities and are affected by the weighted phase space W, which measures the quantity of available channels of the scattering process.[35,61,63] It is surprising that, comparing Fig. 6(b) with (d), acoustic modes with smaller scattering rates at the same frequency have more scattering channels than optical modes, and the overall trend is also contrary to our predictions, which indicates that except for the weighted phase space W, there exist other factors impacting the anharmonic three-phonon scattering rates.

In view of the pretty low lattice conductivity κ_L of CdSe, it is truly rewarding to investigate the electron transport mechanisms and then calculate the corresponding ZT values (the ZT values of CdTe are not as good as those of CdSe and are shown in S1‡), therefore, the Power factor $S^2\sigma$, electronic conductivity κ_e and figure of merit ZT along the a (c) axis of p-type doped CdSe are shown in Fig. 7 (the n-type doped CdSe shows a significantly worse performance, and the relevant ZT values are shown in S2‡) with regard to electronic scattering time τ. We use the formula $\tau \sim d/\upsilon$ to estimate the amplitude of it roughly, where d represents the average electron–electron distance decided by the doping concentration, υ is the electron velocity and can be further written as: $\upsilon = \frac{1}{\hbar}\frac{\partial E(\kappa)}{\partial \kappa}$. For the case of CdSe with a doping concentration of $n \sim 10^{20}$ cm^{-3}, the electron velocity $\upsilon \sim 6 \times 10^4$ m s^{-1} so that the τ is estimated about 15 fs and can be limited to the range of 1–10 fs by referring to literature[12,64,65] and taking the impurity scattering, lattice vibration and other factors into account, in this paper we used 3, 5, 7 and 9 fs for further illustrations. At a temperature of 1200 K, the maximum power factor $S^2\sigma$ is 7.90, 6.14, 4.39 and 2.63 ($\times 10^{-3}$ W m^{-1} K^{-2}) for electronic scattering times of 9 fs, 7 fs, 5 fs and 3 fs, respectively. The change of electronic scattering time has little influence on electronic thermal conductivity κ_e until the doping concentration increases to 3×10^{20} cm^{-3}, because the lattice thermal conductivity κ_L along the a axis of CdSe is smaller and

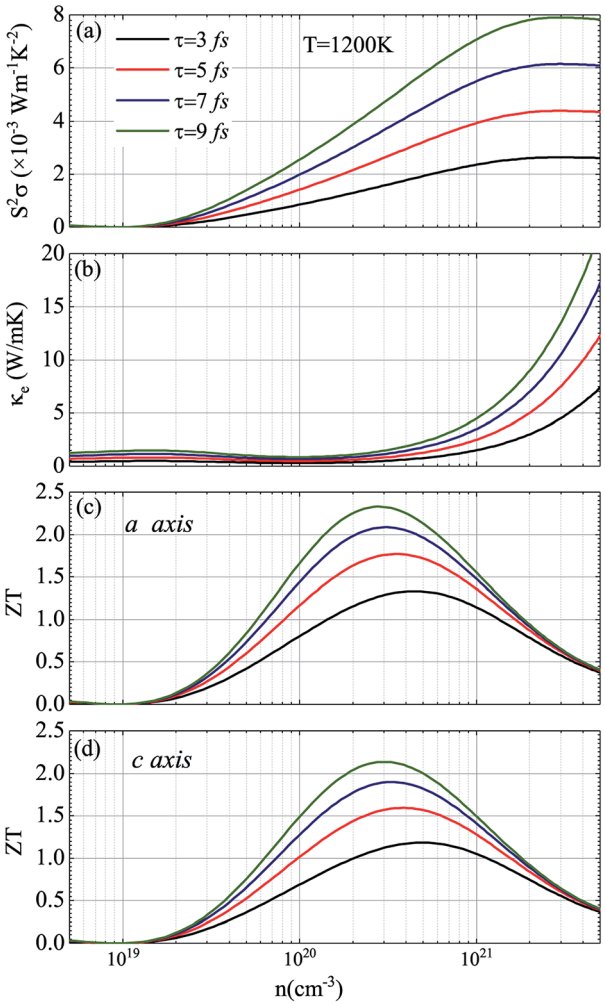

Fig. 7 Thermoelectric parameters of CdSe at 1200 K: (a) power factor $S^2\sigma$, (b) electronic thermal conductivity κ_e, and figure of merit ZT along the a axis (c) and c axis (d). In (a–d) the black, red, blue and green curves represent the electronic scattering times of 3 fs, 5 fs, 7 fs and 9 fs, respectively.

under the same doping concentration and electronic scattering time the relevant TE performance is better. With the electronic scattering τ = 9, 7, 5 and 3 fs, the maximum ZT values are 2.3 ($n = 2.75 \times 10^{20}$ cm^{-3}), 2.1 ($n = 3.09 \times 10^{20}$ cm^{-3}), 1.8 ($n = 3.46 \times 10^{20}$ cm^{-3}) and 1.3 ($n = 4.32 \times 10^{20}$ cm^{-3}) for CdSe-a, respectively. In terms of CdSe-c, the values are slightly smaller but still ideal: 2.2 ($n = 3.09 \times 10^{20}$ cm^{-3}), 1.9 ($n = 3.46 \times 10^{20}$ cm^{-3}), 1.6 ($n = 4.09 \times 10^{20}$ cm^{-3}) and 1.2 ($n = 4.81 \times 10^{20}$ cm^{-3}) for τ = 9, 7, 5 and 3 fs, respectively. All of the above ZT values exceed 1, even for the minimum electronic scattering time $\tau = 3$ fs. Using $\tau = 5$ fs as an example, the ZT value of CdSe is also larger than that of many currently commercially utilized materials, such as $AgSbTe_2$ ($ZT \sim 1.6$),[66,67] Ag_9TiTe_5 and $Yb_xCo_4Sb_{12}$ ($ZT \sim 1.2$).[68,69]

Considering that temperature also plays a critical role in the ZT valus, Fig. 8 shows the corresponding thermoelectric parameters of p-type doped CdSe at different temperatures with

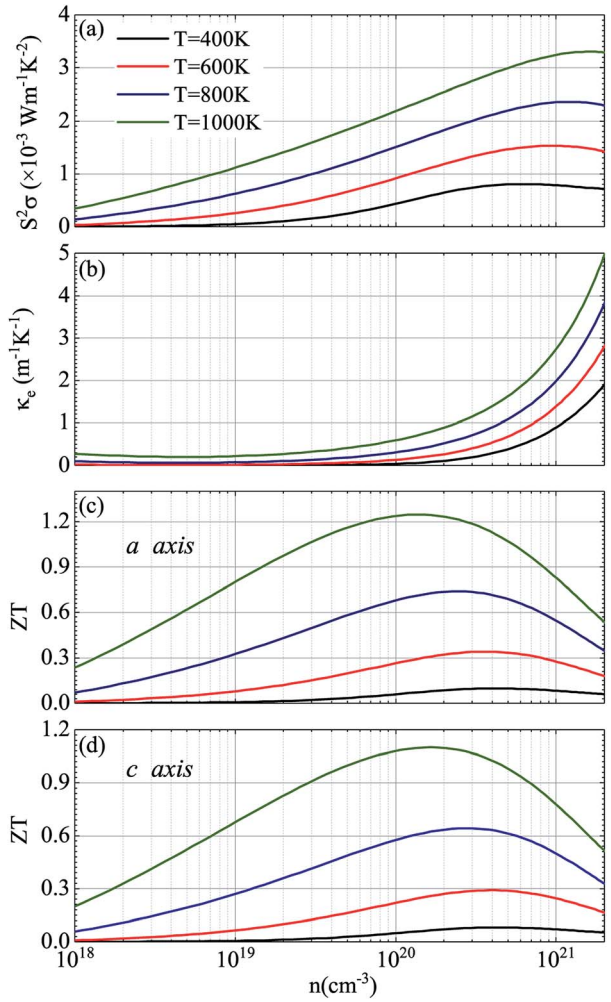

Fig. 8 Thermoelectric parameters of CdSe with the electronic scattering time of 5 fs: (a) power factor $S^2\sigma$, (b) electronic thermal conductivity κ_e, and figure of merit ZT along the a axis (c) and c axis (d). In (a–d), the black, red, blue and green curves represent the temperatures of 400 K, 600 K, 800 K and 1000 K, respectively.

the electronic scattering time of 5 fs. It can be seen from the figure that with the increase of temperature, the doping concentration of the maximum power factor obtained has a less obvious increase, and additionally, there is a slightly decrease in the power factor $S^2\sigma$ compared to the temperature of 1200 K with the same electronic scattering time, and the relevant electronic thermal conductivity κ_e is decreased too. The values of the power factor $S^2\sigma$ are 3.30, 2.36, 1.53 and 0.80 ($\times10^{-3}$ W m^{-1} K^{-2}) for temperatures of 1000 K, 800 K, 600 K and 400 K, respectively, and the figure of merit ZT along the a axis is 1.25 ($n = 1.34 \times 10^{20}$ cm^{-3}), 0.74 ($n = 2.47 \times 10^{20}$ cm^{-3}), 0.34 ($n = 3.55 \times 10^{20}$ cm^{-3}) and 0.10 ($n = 4.19 \times 10^{20}$ cm^{-3}) for temperatures of 1000 K, 800 K, 600 K and 400 K, respectively. The performance of CdSe-c is not good as that of the former, but a value exceeding 1 ($ZT = 1.10$) was still obtained at 1000 K with a doping concentration of 1.83×10^{20} cm^{-3}. Compared with those materials that have equivalent ZT values, such as NbFeSb-based p-type half-Heuslers ($ZT \sim 1$)[69] and $Cu_{2.1}Zn_{0.9}SnSe_4$ ($ZT \sim 0.9$),[70] CdSe is easy to obtain and more economical and practical, and the anisotropic behavior of it can be achieved experimentally by using the perfect monocrystal. According to Fig. 7 and 8, the final figure of merit ZT is the result of mutual restriction of thermopower S, electrical conductivity σ, temperature T, electronic thermal conductivity κ_e and lattice thermal conductivity κ_L. So finding the best combination of them is the key to acquiring the optimal ZT values. Our research suggests that CdSe is not only a prominent photoelectric material, but also has excellent performance in the field of thermoelectricity, and combining these two properties with practical applications will make them a better prospect.

4. Conclusion

In summary, we have investigated the thermal transport properties and electronic structure of anisotropic ZnSe and CdSe and isotropic ZnTe and CdTe by taking advantage of first-principles calculations. Regarding the former the thermoelectric performance along the a axis is relatively better, and CdTe and CdSe have the lower lattice thermal conductivities κ_L among the four materials, which are 6.14 W m^{-1} K^{-1} and 3.85 W m^{-1} K^{-1} (a axis) at room temperature, respectively. Inspired by the pretty low lattice thermal conductivity of CdSe, we calculated the power factor $S^2\sigma$, electronic thermal conductivity κ_e and finally obtained the figure of merit ZT based on the Boltzmann transport equation. At a temperature of 1200 K, the ZT value of CdSe along the a axis (c axis) is 1.8 (1.6) with the electronic scattering time of 5 fs, and it has better properties than most of the materials currently studied and commercially applied. These direct band gap semiconductors are well known for their excellent photoelectric performance, while the thermoelectric properties are usually ignored, however, our studies reveal more possibilities of them in the area of thermoelectricity, and in order to obtain broader application prospects we will focus on the combination of photoelectric properties and thermoelectric properties in a later investigation.

Conflicts of interest

There are no conflicts to declare.

Acknowledgements

This research were supported by the National Natural Science Foundation of China under Grant No. 11774396 and No. 11704322, the Shandong Natural Science Funds for Doctoral Program under Grant No. ZR2017BA017, and the National Key Research and Development Program of China under Grant No. 2016YFA0300902.

References

1 J. P. Heremans, V. Jovovic, E. S. Toberer, A. Saramat, K. Kurosaki, A. Charoenphakdee, S. Yamanaka and G. J. Snyder, *Science*, 2008, **321**, 554.

2 G. J. Snyder and E. S. Toberer, in *Materials For Sustainable Energy: A Collection of Peer-Reviewed Research and Review Articles from Nature Publishing Group*, World Scientific, 2011, pp. 101–110.
3 L. E. Bell, *Science*, 2008, **321**, 1457.
4 J. P. Heremans, M. S. Dresselhaus, L. E. Bell and D. T. Morelli, *Nat. Nanotechnol.*, 2013, **8**, 471.
5 G. Melnyk, E. Bauer, P. Rogl, R. Skolozdra and E. Seidl, *J. Alloys Compd.*, 2000, **296**, 235.
6 K. Biswas, J. He, I. D. Blum, C.-I. Wu, T. P. Hogan, D. N. Seidman, V. P. Dravid and M. G. Kanatzidis, *Nature*, 2012, **489**, 414.
7 H. Wang, J.-H. Bahk, C. Kang, J. Hwang, K. Kim, J. Kim, P. Burke, J. E. Bowers, A. C. Gossard, A. Shakouri, *et al.*, *Proc. Natl. Acad. Sci. U. S. A.*, 2014, **111**, 10949.
8 L. Hicks and M. S. Dresselhaus, *Phys. Rev. B: Condens. Matter Mater. Phys.*, 1993, **47**, 12727.
9 Y. Pei, A. LaLonde, S. Iwanaga and G. J. Snyder, *Energy Environ. Sci.*, 2011, **4**, 2085.
10 Y. Zhao and Z. Dai, *RSC Adv.*, 2017, **7**, 25803.
11 W. Liu, X. Tan, K. Yin, H. Liu, X. Tang, J. Shi, Q. Zhang and C. Uher, *Phys. Rev. Lett.*, 2012, **108**, 166601.
12 Y. Zhao, Z. Dai, C. Zhang, C. Lian, S. Zeng, G. Li, S. Meng and J. Ni, *Phys. Rev. B*, 2017, **95**, 014307.
13 J. Shuai, J. Mao, S. Song, Q. Zhu, J. Sun, Y. Wang, R. He, J. Zhou, G. Chen, D. J. Singh, *et al.*, *Energy Environ. Sci.*, 2017, **10**, 799.
14 J. Mao, Y. Wu, S. Song, Q. Zhu, J. Shuai, Z. Liu, Y. Pei and Z. Ren, *ACS Energy Lett.*, 2017, **2**, 2245.
15 M. Zebarjadi, G. Joshi, G. Zhu, B. Yu, A. Minnich, Y. Lan, X. Wang, M. Dresselhaus, Z. Ren and G. Chen, *Nano Lett.*, 2011, **11**, 2225.
16 Y. Pei, H. Wang and G. J. Snyder, *Adv. Mater.*, 2012, **24**, 6125.
17 Y. Pei, X. Shi, A. LaLonde, H. Wang, L. Chen and G. J. Snyder, *Nature*, 2011, **473**, 66.
18 K. F. Hsu, S. Loo, F. Guo, W. Chen, J. S. Dyck, C. Uher, T. Hogan, E. K. Polychroniadis and M. G. Kanatzidis, *Science*, 2004, **303**, 818.
19 K. Biswas, J. He, Q. Zhang, G. Wang, C. Uher, V. P. Dravid and M. G. Kanatzidis, *Nat. Chem.*, 2011, **3**, 160.
20 B. Poudel, Q. Hao, Y. Ma, Y. Lan, A. Minnich, B. Yu, X. Yan, D. Wang, A. Muto, D. Vashaee, X. Chen, J. Liu, M. S. Dresselhaus, G. Chen and Z. Ren, *Science*, 2008, **320**, 634.
21 L.-D. Zhao, X. Zhang, H. Wu, G. Tan, Y. Pei, Y. Xiao, C. Chang, D. Wu, H. Chi, L. Zheng, *et al.*, *J. Am. Chem. Soc.*, 2016, **138**, 2366.
22 P. Popov, P. Fedorov and V. Konyushkin, *Dokl. Phys.*, 2008, **53**, 353.
23 P. Popov, P. Fedorov and V. Osiko, *Phys. Solid State*, 2010, **52**, 504.
24 P. Popov, P. Fedorov, V. Konyushkin, A. Nakladov, S. Kuznetsov, V. Osiko and T. Basiev, in *Doklady Physics*, vol. 53, Springer, 2008, pp. 413–415.
25 Q. Zhang, Y. Sun, W. Xu and D. Zhu, *Adv. Mater.*, 2014, **26**, 6829.
26 Q. Jin, S. Jiang, Y. Zhao, D. Wang, J. Qiu, D.-M. Tang, J. Tan, D.-M. Sun, P.-X. Hou, X.-Q. Chen, *et al.*, *Nat. Mater.*, 2019, **18**, 62.
27 D. Parker and D. J. Singh, *Phys. Rev. B: Condens. Matter Mater. Phys.*, 2010, **82**, 035204.
28 J. N. Kim, M. Kaviany and J.-H. Shim, *Phys. Rev. B*, 2016, **93**, 075119.
29 R. Guo, X. Wang, Y. Kuang and B. Huang, *Phys. Rev. B: Condens. Matter Mater. Phys.*, 2015, **92**, 115202.
30 A. Olvera, N. Moroz, P. Sahoo, P. Ren, T. Bailey, A. Page, C. Uher and P. Poudeu, *Energy Environ. Sci.*, 2017, **10**, 1668.
31 W. Xie, X. Tang, Y. Yan, Q. Zhang and T. M. Tritt, *Appl. Phys. Lett.*, 2009, **94**, 102111.
32 P. Reiss, J. Bleuse and A. Pron, *Nano Lett.*, 2002, **2**, 781.
33 M. Gao, S. Kirstein, H. Möhwald, A. L. Rogach, A. Kornowski, A. Eychmüller and H. Weller, *J. Phys. Chem. B*, 1998, **102**, 8360.
34 B. Liao, J. Zhou, B. Qiu, M. S. Dresselhaus and G. Chen, *Phys. Rev. B: Condens. Matter Mater. Phys.*, 2015, **91**, 235419.
35 Y. Zhao, Z. Dai, C. Lian, S. Zeng, G. Li, J. Ni and S. Meng, *Phys. Rev. Mater.*, 2017, **1**, 065401.
36 W. Li, J. Carrete, N. A. Katcho and N. Mingo, *Comput. Phys. Commun.*, 2014, **185**, 1747.
37 P. Vogt, P. De Padova, C. Quaresima, J. Avila, E. Frantzeskakis, M. C. Asensio, A. Resta, B. Ealet and G. Le Lay, *Phys. Rev. Lett.*, 2012, **108**, 155501.
38 G. Kresse and J. Furthmüller, *Phys. Rev. B: Condens. Matter Mater. Phys.*, 1996, **54**, 11169.
39 A. Togo, F. Oba and I. Tanaka, *Phys. Rev. B: Condens. Matter Mater. Phys.*, 2008, **78**, 134106.
40 G. Kresse and D. Joubert, *Phys. Rev. B: Condens. Matter Mater. Phys.*, 1999, **59**, 1758.
41 J. P. Perdew, A. Ruzsinszky, G. I. Csonka, O. A. Vydrov, G. E. Scuseria, L. A. Constantin, X. Zhou and K. Burke, *Phys. Rev. Lett.*, 2008, **100**, 136406.
42 G. K. Madsen and D. J. Singh, *Comput. Phys. Commun.*, 2006, **175**, 67.
43 X. Yang, Y. Zhao, Z. Dai, M. Zulfiqar, J. Zhu and J. Ni, *Phys. Lett. A*, 2017, **381**, 3514.
44 Y. Ding and Y. Wang, *Appl. Surf. Sci.*, 2017, **396**, 1164.
45 W. Li and N. Mingo, *Phys. Rev. B: Condens. Matter Mater. Phys.*, 2014, **90**, 094302.
46 A. Haloui, Y. Feutelais and B. Legendre, *J. Alloys Compd.*, 1997, **260**, 179.
47 A. Štajn, R. Žikić, B. Ognjanović, Z. Saičić, S. Z. Pavlović, M. Kostić and V. M. Petrović, *Comp. Biochem. Physiol., Part C: Pharmacol., Toxicol. Endocrinol.*, 1997, **117**, 167.
48 R. Sharma and Y. Chang, *J. Phase Equilib.*, 1989, **10**, 334.
49 R. Sharma and Y. Chang, *J. Phase Equilib.*, 1996, **17**, 155.
50 C. Okoye, *Phys. B*, 2003, **337**, 1.
51 E. Deligoz, K. Colakoglu and Y. Ciftci, *Phys. B*, 2006, **373**, 124.
52 O. Zakharov, A. Rubio, X. Blase, M. L. Cohen and S. G. Louie, *Phys. Rev. B: Condens. Matter Mater. Phys.*, 1994, **50**, 10780.
53 P. K. Sarswat, S. Sarkar, G. Yi and M. L. Free, *J. Phys. Chem. C*, 2017, **121**, 18263.
54 T. Nakashima and Y. Umakoshi, *Philos. Mag. Lett.*, 1992, **66**, 317.

55 B. Peng, H. Zhang, H. Shao, Y. Xu, X. Zhang and H. Zhu, *RSC Adv.*, 2016, **6**, 5767.
56 L. Lindsay, D. Broido and T. Reinecke, *Phys. Rev. Lett.*, 2013, **111**, 025901.
57 A. Jain and A. J. McGaughey, *Sci. Rep.*, 2015, **5**, 8501.
58 D. K. Efetov and P. Kim, *Phys. Rev. Lett.*, 2010, **105**, 256805.
59 B. Mortazavi, O. Rahaman, T. Rabczuk and L. F. C. Pereira, *Carbon*, 2016, **106**, 1.
60 B. Peng, H. Zhang, H. Shao, Y. Xu, R. Zhang, H. Lu, D. W. Zhang and H. Zhu, *ACS Appl. Mater. Interfaces*, 2016, **8**, 20977.
61 W. Li and N. Mingo, *Phys. Rev. B: Condens. Matter Mater. Phys.*, 2014, **89**, 184304.
62 S. Sarkar, P. K. Sarswat, S. Saini, P. Mele and M. L. Free, *Sci. Rep.*, 2019, **9**, 8180.
63 W. Li and N. Mingo, *Phys. Rev. B: Condens. Matter Mater. Phys.*, 2015, **91**, 144304.
64 X. Yang, Z. Dai, Y. Zhao, J. Liu and S. Meng, *J. Phys.: Condens. Matter*, 2018, **30**, 425401.
65 X. Tan, W. Liu, H. Liu, J. Shi, X. Tang and C. Uher, *Phys. Rev. B: Condens. Matter Mater. Phys.*, 2012, **85**, 205212.
66 H. Wang, J.-F. Li, M. Zou and T. Sui, *Appl. Phys. Lett.*, 2008, **93**, 202106.
67 D. Morelli, V. Jovovic and J. Heremans, *Phys. Rev. Lett.*, 2008, **101**, 035901.
68 K. Kurosaki, A. Kosuga, H. Muta, M. Uno and S. Yamanaka, *Appl. Phys. Lett.*, 2005, **87**, 061919.
69 G. Joshi, R. He, M. Engber, G. Samsonidze, T. Pantha, E. Dahal, K. Dahal, J. Yang, Y. Lan, B. Kozinsky, *et al.*, *Energy Environ. Sci.*, 2014, **7**, 4070.
70 M.-L. Liu, I.-W. Chen, F.-Q. Huang and L.-D. Chen, *Adv. Mater.*, 2009, **21**, 3808.